JOURNAL OF SOLID STATE CHEMISTRY 71, 305–323 (1987)

X-Ray Microanalysis and High-Resolution Transmission Electron Microscopy of the Reduced Titanium–Niobium Oxides

S. K. E. FORGHANY*

Inorganic Chemistry Laboratory, University of Oxford, Oxford, United Kingdom

A. K. CHEETHAM

Chemical Crystallography Laboratory, University of Oxford, Oxford, United Kingdom

AND A. OLSEN

Institute of Physics, University of Oslo, Oslo, Norway

Received August 19, 1986; in revised form December 24, 1986

Phase relationships in $TiNb_2O_7$ and $Ti_2Nb_{10}O_{29}$ reductions at 1400°C were investigated by means of X-ray microanalytical electron microscopy and high-resolution transmission electron microscopy (TEM). Compositions of phases present in equilibrium were obtained by applying thin-crystal approximation by which Nb/Ti ratios in different phases were determined; their oxygen content was inferred from structural considerations. In this manner, phase relationships in that portion of the TiO_2–NbO_2–$NbO_{2.5}$ equilibrium diagram with $2.417 \geq x$ (in MeO_x) ≥ 2 were defined. Data obtained, in combination with high-resolution electron microscopy observations, confirmed that the reduction reaction, in part, is a heterogeneous process controlled by outward diffusion of both metal and oxygen atoms. Recombination of the diffused particles leads to the formation of separate crystals. The original block structure phase undergoes transformation in a quasihomogeneous manner either to an isomorphous phase in the binary Nb–O system or to a structurally related lower composition oxide. A new superstructure $Me_{25}O_{60}(Ti_{7.16}Nb_{42.84}O_{120})$ has been detected as an intermediate metastable phase, generated in the reduction of $TiNb_2O_7$ to stable $Me_{12}O_{29}(Ti_{1.53}Nb_{10.47}O_{29})$ and $MeO_2(Ti_{0.52}Nb_{0.48}O_2)$ phases. Consideration of phase relationships among $Me_{25}O_{60}$, $Me_{12}O_{29}$, and MeO_2 suggests a chemical mechanism for the reaction concerned. The $Me_{25}O_{60}$ superstructure has a monoclinic symmetry with cell parameters $a = 19.0$ Å, $b = 3.8$ Å, $c = 26.6$ Å, $\alpha = 90°$, $\beta = 90°$, $\gamma = 78.5°$, as determined from the structure image calculations.

Introduction

In the system TiO_2–Nb_2O_5, three distinct phases, $TiNb_2O_7$, $Ti_2Nb_{10}O_{29}$, and $TiNb_{24}O_{62}$, are present (*1*). These oxides adopt "block"-type structures (*2–5*) with Ti(IV) mainly occupying corner and edge sites of the blocks (*6*). Phase equilibria in the system TiO_2–NbO_2–$NbO_{2.5}$ have previously been investigated at 1400°C under controlled atmospheres using CO/CO_2 buffers (*7, 8*). In the reduction of $TiNb_2O_7$

* To whom all correspondence should be addressed at Hoogovens Groep BV, Research and Development Laboratories, Department of Surface Technology, P.O. Box 10000, 1970 CA IJmuiden, The Netherlands.

0022-4596/87 $3.00

and $Ti_2Nb_{10}O_{29}$ to their respective rutile solid solutions ($Ti_xNb_{1-x}O_2$; $x = 0.33$ and $x = 0.16$ respectively), the (p, x) isotherms showed bivariant characteristics with the exception of a narrow univariant step at log p_{O_2} (atm = ca. −9.0. This bivariance arises from coherent intergrowth of intermediate block structure phases, while the univariant plateau occurs where the three solid phases Me_3O_7, $Me_{12}O_{29}$, and MeO_2 (Me = Nb, Ti) coexist. In the course of the reductions, a second phase is generated which is richer in titanium than the original materials. Throughout the reduction of $TiNb_2O_7$, a rutile phase (MeO_2) is present in equilibrium with the block structure phase. In the reduction of $Ti_2Nb_{10}O_{29}$, however, Me_3O_7 is formed initially, but the rutile phase forms on further reduction.

Quantitative phase analysis in the earlier work involved conventional X-ray powder diffraction analysis. In the present work, we apply a combination of analytical electron microscopy and high-resolution transmission electron microscopy to studies of the reduced titanium–niobium oxides. Analytical electron microscopy is an excellent tool for quantitative characterization of polycrystalline mixtures (*9*) since it provides a means for analyzing individual crystallites of the constituent phases. Applying this technique, we have determined the compositions of phases present during the reductions of $TiNb_2O_7$ and $Ti_2Nb_{10}O_{29}$, thereby defining the phase relationships in part of the ternary phase diagram TiO_2–NbO_2–$NbO_{2.5}$ for MeO_x; $2 \leq x \leq 2.417$. High-resolution transmission electron microscopy, on the other hand, provides the possibility for studying the link between the microstructure of intermediate oxides and the thermodynamics of the system, as has already been reported for the reduction of $TiNb_{24}O_{62}$ (*8*). In addition, direct information on the mechanisms of solid state reactions can be obtained and this we elucidate for the reduction of $TiNb_2O_7$ to $Me_{12}O_{29}$ and MeO_2 via a metastable transient superstructure $Me_{25}O_{60}$.

Experimental

Specimen preparation. The reduced titanium–niobium oxides where the same as used in previous work (*7*). In brief, the oxides were prepared by reduction of $TiNb_2O_7$ and $Ti_2Nb_{10}O_{29}$ at 1400°C under controlled oxygen fugacities generated from metered CO/CO_2 mixtures. The reduction experiments were carried out in a horizontal quench furnace (*10*), permitting rapid heating/quenching of the materials *in vacuo* or in an inert gas environment. The oxygen/total metal ratios of the oxides were determined by gravimetric reoxidation to $TiO_2 \cdot Nb_2O_5$, using a Cahn RG4 electrobalance.

Analytical electron microscopy. Analytical electron microscopy was performed in a JEOL 100CX TEMSCAN system with a Li-drifted silicon X-ray detector. X-ray emission spectra were obtained in the SEM mode of the microscope. This permitted (1) the avoidance of error due either to overlapped crystallites or to nearby particles and supporting grid bars, all of which can contribute to X-ray spectra, and (2) monitoring the crystallite size, thereby minimizing absorption and fluorescence effects, which depend on the particle size and orientation. Smaller crystallites, free from other particles and not lying close to or on copper grid bars, were preferentially selected. Although there is no way of assessing crystal transparency to primary X-rays in the SEM mode of the microscope, an empirical method similar to the one described in Ref. (*9*) was adopted in the present work, which enabled us to gauge crystal thicknesses. According to the present method, the relative intensities of two lines with high- and low-absorption cross sections of a constituent element in the crystallite is dependent upon the crystallite thickness. Hence, by calibrating with

a standard specimen with known composition, it is possible to probe crystal thickness of materials having unknown compositions. Thicker crystals require corrections for absorption and fluorescence effects. In general, absorption effects are significant when using emission lines with large differences between their mass absorption coefficients. Fluorescence effects, on the other hand, lead to additional X-ray intensity, generated by the specimen, supporting the grid and the microscope components. The latter two are less critical and can be minimized experimentally, but for crystals containing elements with small differences in their atomic numbers, the fluorescence effect can be pronounced.

In the thin-crystal approximation, however, X-ray absorption and fluorescence effects can be neglected because the crystal is assumed to be transparent to the primary X rays produced by the incident beam. In this approximation, the ratio of the characteristic X-ray intensities for any two elements measured simultaneously by an energy dispersive detector is proportional to the ratio of their weight fractions (*11*):

$$C_A/C_B = k_{AB} \cdot I_A/I_B, \qquad (1)$$

where I_A and I_B are the observed intensities and C_A and C_B are the weight fractions of elements A and B. The correction factor k_{AB} is a constant for a particular instrument detector and can be determined from standard specimens. In the present work, crystals were studied with an area scan of approximately 0.003 μm and with a counting time of 100 sec, so that average composition information could be obtained from a large volume of crystals. From each sample, up to 30 crystallites were examined. A typical spectrum is shown in Fig. 1. The thickness of the crystal was monitored from the magnitude of the intensity ratio I(NbL)/I(Nb$K\alpha$). The L line has a high-absorption cross section (Table I) and data in which the above ratio fell below 2.50 were rejected. The ratio I(NbL)/I(Nb$K\alpha$) characteristically occurs in the range of 2.50–3.00 for thin crystals, that is, for a thickness less than 100 nm. For quantitative analysis, the ratio I(NbL)/I(Ti$K\alpha$) gave more consistent results than the ratio I(Nb$K\alpha$)/I(Ti$K\alpha$).

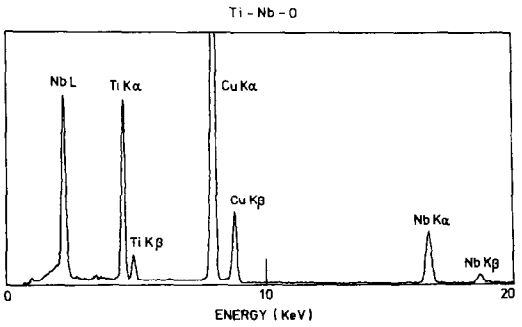

FIG. 1. A typical X-ray emission spectrum of a titanium–niobium oxide at 100 kV (counting time: 100 sec). A Cu specimen-supporting grid was used.

TABLE I

X-RAY ABSORPTION COEFFICIENTS (FROM REF. (*12*))

Line	Absorption by Nb	Absorption by Ti
Nb$L\alpha$	783.0	819.6
Nb$L\beta$	703.2	732.1
Nb$K\alpha$	20.4	27.9
Ti$K\alpha$	718.7	110.6
Nb$K\beta$	563.6	86.7

The proportionality constant, $k_{Nb,Ti}$, was determined by analyzing well-characterized standard samples of $TiNb_2O_7$ and $Ti_2Nb_{10}O_{29}$. Of the former, 12 crystallites gave a mean k value of 0.706. From the latter, 12 crystallites yielded an average value of 0.721. A mean $k_{Nb,Ti}$ value of 0.714 was adopted for all subsequent analyses, and the atomic ratio of niobium to titanium, n_{Nb}/n_{Ti}, was obtained from the relation

$$n_{Nb}/n_{Ti} = 0.714 \times I(\text{Nb}L)/I(\text{Ti}K\alpha). \qquad (2)$$

High-resolution transmission electron microscopy and theoretical calculations. For high-resolution transmission electron microscopy of the reduced titanium–niobium oxides, intermediate oxides of

$TiNb_2O_7$ were selected at different stages of the reduction. Experiments were carried out in a Siemens Elmiskope 102 electron microscope and (*h01*) lattice images of block structure phases were obtained, by standard procedures, from thin (<10-nm) edges of crystal fragments, at 70–90 nm underfocus. Theoretical simulations of the electron micrographs involved application of the multislice method for dynamical electron scattering (*13, 14*). Computer programs (*15*) of the Arizona State University were utilized in all calculations reported in the present work. Details of the calculations are discussed in Section III under Results.

Results

I. Analytical Electron Microscopy

Analytical electron microscopy results for the reduced titanium–niobium oxides are summarized in Table II. To define phase relationships at different stages of the reduction, the data in Table II are expressed in terms of formulae described in previous work (*7*). The compositions of the coexisting phases are given in Table III and the corresponding tie lines are drawn in the ternary phase diagram TiO_2–NbO_2–$NbO_{2.5}$ for MeO_x, $2 \leq x \leq 2.417$. The diagram (Fig. 2) consists of three parts: (i) the initial stages of bivariant reductions of $TiNb_2O_7$ and $Ti_2Nb_{10}O_{29}$, (ii) the univariant triangle area formed at isobar log p_{O_2} (atm) = ca. −9.0, and (iii) the second stages of bivariant reductions of the oxides. The tie lines assigned to different parts of the diagram are discussed below:

(i) The first stages of the bivariant reductions of $TiNb_2O_7$ and $Ti_2Nb_{10}O_{29}$ extend to the limiting compositions of about $MeO_{2.24}$ and $MeO_{2.37}$ at oxygen fugacity log p_{O_2} (atm) = ca. −9.0. The bivariance in both reductions arise from partial transformations of the double oxides to their isomorphous

TABLE II

ANALYTICAL ELECTRON MICROSCOPY DATA FOR REDUCTIONS OF $TiNb_2O_7$ AND $Ti_2Nb_{10}O_{29}$ AT 1400°C, GROUPED ACCORDING TO THE PHASES PRESENT AT EACH STAGE

		$Ti_{1-x}Nb_{2+x}O_7$		$Ti_{2-x}Nb_{10+x}O_{29}$		$Ti_xNb_{1-x}O_2$		Others	
−log p_{O_2} (atm)	x in MeO_x (Me = Ti, Nb)	Nb/Ti	No. of crystals	Nb/Ti	No. of crystals	Nb/Ti	No. of crystals	Nb/Ti	No. of crystals
6.29	2.324	2.19	9	—	—	—	—	—	—
7.17	2.320	2.25	22	—	—	—	—	—	—
7.77	2.313	2.33	9	—	—	—	—	3.35	1
7.78	2.408[a]	2.48	1	5.51	10	—	—	—	—
8.42	2.273	2.78	15	—	—	0.56	1	—	—
8.42	2.395[a]	2.88	3	5.95	15	—	—	—	—
9.27	2.375[a]	—	—	6.90	18	—	—	3.60 5.39	8 6
9.6	2.344[a]	—	—	9.09	11	—	—	4.28 5.99	7 3
10.3	2.055	—	—	10.37	1	1.72	3	—	—
10.3	2.294[a]	—	—	10.60	11	1.80	2	—	—
10.8	2.215[a]	—	—	14.79	7	2.73	8	$Nb_{12}O_{29}$	2
11.4	2.005[a]	—	—	—	—	4.98	17	—	—

[a] Starting material $Ti_2Nb_{10}O_{29}$.

TABLE III

QUANTITATIVE PHASE RELATIONSHIPS AT DIFFERENT STAGES OF $TiNb_2O_7$ AND $TiNb_{10}O_{29}$ REDUCTIONS AT 1400°C

$-\log p_{O_2}$ (atm)	x in MeO_x (Me = Ti, Nb)	Coexisting phases (mole/$TiNb_2O_7$ or $Ti_2Nb_{10}O_{29}$ starting materials)
6.29	2.324	$0.09(Ti_{0.98}Nb_{0.02}O_2)$ + $0.97(\mathbf{Ti_{0.94}Nb_{2.06}O_7})$
7.17	2.320	$0.12(Ti_{0.97}Nb_{0.03}O_2)$ + $0.96(\mathbf{Ti_{0.92}Nb_{2.08}O_7})$
7.77	2.313	$0.18(Ti_{0.88}Nb_{0.12}O_2)$ + $0.94(\mathbf{Ti_{0.90}Nb_{2.10}O_7})$
7.78	2.408[a]	$0.40(\mathbf{Ti_{0.86}Nb_{2.14}O_7})$ + $0.90(\mathbf{Ti_{1.84}Nb_{10.16}O_{29}})$
8.42	2.273	$0.54(\mathbf{Ti_{0.64}Nb_{0.36}O_2})$ + $0.82(\mathbf{Ti_{0.79}Nb_{2.21}O_7})$
8.42	2.395[a]	$0.80(\mathbf{Ti_{0.77}Nb_{2.23}O_7})$+$0.80(\mathbf{Ti_{1.73}Nb_{10.27}O_{29}})$
9.0[b]	2.244	$0.87(Ti_{0.56}Nb_{0.44}O_2)$ + $0.71(Ti_{0.72}Nb_{2.28}O_7)$
9.0[b]	2.387[a]	$0.89(Ti_{0.56}Nb_{0.44}O_2)$ + $0.93(Ti_{1.62}Nb_{10.38}O_{29})$
9.27	2.375[a]	$1.20(Ti_{0.53}Nb_{0.47}O_2)$ + $0.90(\mathbf{Ti_{1.52}Nb_{10.48}O_{29}})$
9.6	2.344[a]	$2.03(Ti_{0.50}Nb_{0.50}O_2)$ + $0.83(\mathbf{Ti_{1.19}Nb_{10.81}O_{29}})$
10.3	2.055	$2.71(\mathbf{Ti_{0.36}Nb_{0.64}O_2})$ + $0.03(\mathbf{Ti_{1.04}Nb_{10.96}O_{29}})$
10.3	2.294[a]	$3.51(\mathbf{Ti_{0.36}Nb_{0.64}O_2})$ + $0.71(\mathbf{Ti_{1.04}Nb_{10.96}O_{29}})$
10.8	2.215[a]	$6.00(\mathbf{Ti_{0.27}Nb_{0.73}O_2})$ + $0.50(\mathbf{Ti_{0.76}Nb_{11.24}O_{29}})$
11.4	2.005[a]	$(\mathbf{Ti_{0.17}Nb_{0.83}O_2})$

Note. Solid solution phases identified by analytical microscopy are boldface.

[a] Starting material $Ti_2Nb_{10}O_{29}$.

[b] Data for isobar log p_{O_2} (atm) = −9.0, are quoted from Ref. (*7*).

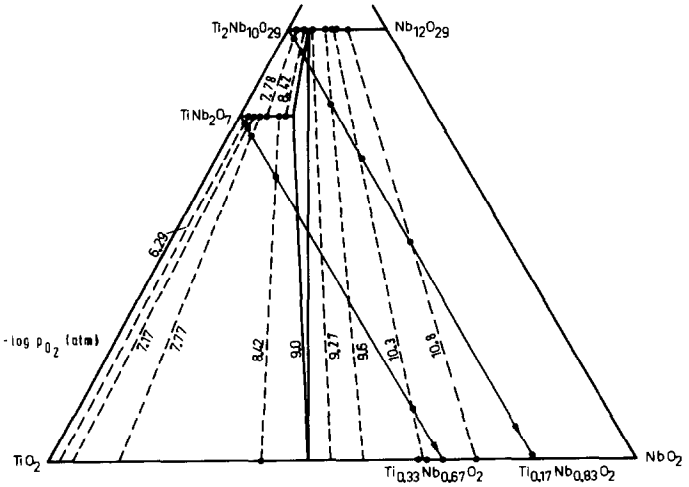

FIG. 2. Gibbs triangle representation of phase relations in the system TiO_2–NbO_2–$NbO_{2.5}$ at 1400°C, ratio of oxygen/total metal ≤2.417. Tie lines depicting equilibrium coexistence of condensed phases at various oxygen fugacities are shown by broken lines. Solid lines represent boundaries between two or three phase areas. Solid circles indicate experimental data points, obtained from analytical microscopy and from thermogravimetric analysis of whole specimens. The reduction trajectories of $Ti_2Nb_{10}O_{29}$ and $TiNb_2O_7$ are shown by arrows.

phases in the binary Nb–O system. $Ti_2Nb_{10}O_{29}$ transforms to the mixed valence $Nb_{12}O_{29}$ and the two phases are completely miscible, but substitution of Nb(IV) for Ti(IV) in $TiNb_2O_7$ takes place only to the limiting composition $Ti_{0.72}Nb_{2.28}O_7$ at log p_{O_2} (atm) = ca. −9.0; pure Nb_3O_7 is unknown (*16*). In each system, a second phase is also generated which initially has a higher Ti/Nb ratio than that in the original block structure compounds. As reductions of the oxides proceed further at lower oxygen fugacities, both the original and the second phases are progressively enriched in niobium, as can be seen from the shape and spread of tie lines in the diagram.

In the reduction of $TiNb_2O_7$, Me_3O_7 (i.e., $TiNb_2O_7$–Nb_3O_7 solid solutions) coexists with MeO_2 (that is, TiO_2–NbO_2 solid solutions) which is the rejected phase. Four tie lines assigned for this stage of the reduction stem from microanalysis of specimen MeO_x, x = 2.324, 2.320, 2.313, and 2.273. It is apparent that in the lightly reduced oxides, the ratio of rutile phase to block structure phase is very small, as we first detect it with a composition $Ti_{0.64}Nb_{0.36}O_2$ in sample, $MeO_{2.273}$ at log p_{O_2} (atm) = −8.42. In the case of the $Ti_2Nb_{10}O_{29}$ reduction, $Me_{12}O_{29}$ (i.e., $Ti_2Nb_{10}O_{29}$–$Nb_{12}O_{29}$ solid solution) coexists in equilibrium with Me_3O_7, which is the second phase in this reduction. Two tie lines are assigned at isobars log p_{O_2} (atm) = −7.78 and −8.42. Because the $Me_{12}O_{29}$ and Me_3O_7 phases are structurally related, some degree of mutual intergrowth in terms of Wadsley defects might be expected, but substantial intergrowth is ruled out since we observed no crystallites with Nb/Ti ratios in the range 3.7–5.0.

(ii) On further reduction of $Ti_2Nb_{10}O_{29}$ at oxygen fugacities below log p_{O_2} (atm) = ca. −9.0, $Me_{12}O_{29}$ occurs in equilibrium with MeO_2 phase, not with Me_3O_7. Likewise, on continued reduction of $TiNb_2O_7$ below this oxygen fugacity, $Me_{12}O_{29}$ is generated in equilibrium with MeO_2 and this would imply that the stability range of the Me_3O_7 solid solution extends as far as log p_{O_2} (atm) = ca. −9.0. From this, it was deduced that at about log p_{O_2} (atm) = −9.0 isobar, three phases, $Me_{12}O_{29}$, Me_3O_7, and MeO_2, coexist in equilibrium, forming a univariant triangle. The three coexisting phases are $Ti_{1.62}Nb_{10.38}O_{29}$, $Ti_{0.72}Nb_{2.28}O_7$, and $Ti_{0.56}Nb_{0.44}O_2$.

(iii) In the second stage of the bivariant reduction of $Ti_2Nb_{10}O_{29}$ and $TiNb_2O_7$, the block structure phase is continuously depleted in titanium. At the same time, the rutile phase moves steadily to the final compositions, $Ti_{0.33}Nb_{0.67}O_2$ and $Ti_{0.17}Nb_{0.83}O_2$, corresponding to complete reductions of $TiNb_2O_7$ and $Ti_2Nb_{10}O_{29}$, respectively. Five tie lines were assigned at isobars log p_{O_2} (atm) = −9.27, −9.6, −10.3, −10.8, and −11.4. Details of their measurements are described below. Specimen $MeO_{2.375}$ is obtained from the reduction of $Ti_2Nb_{10}O_{29}$ at log p_{O_2} (atm) = −9.27, and its microanalysis shows that a $Me_{12}O_{29}$ phase having an average ratio Nb/Ti = 6.90 occurs as the predominant phase. This specimen also contains several impurity crystals which could be grouped in two different compositions, Nb/Ti ≃ 3.60 and Nb/Ti ≃ 5.39. No direct measurement of the rutile phase could be made, since its quantity was low and the crystallites were probably too small to be detected by microscopy. This tie line is constructed on the basis of the composition of $Me_{12}O_{29}$ phase which indicates the equilibrium coexistence of $Ti_{1.52}Nb_{10.48}O_{29}$ with $Ti_{0.53}Nb_{0.47}O_2$. In addition, the tie line intersects the reduction trajectory for $TiNb_2O_7$ at a point corresponding to an oxide with O/*Me* ~ 2.20. An almost isobarically reduced $TiNb_2O_7$ specimen, at log p_{O_2} (atm) = −9.30, had a composition $MeO_{2.200}$. Because in this material, i.e., $MeO_{2.200}$, the coexisting phases $Me_{12}O_{29}$ and MeO_2 occur almost in equal quantities, the specimen was further studied by X-ray powder diffraction and high-resolution transmission electron

microscopy. Findings by both techniques are discussed in the following section. In brief, a Guinier X-ray powder diffraction pattern taken from the oxide clearly revealed the coexistence of o-$Me_{12}O_{29}$ and MeO_2 phases. Reflections of the latter phase could qualitatively be compared with the characteristic lines of a standard $Ti_{0.50}Nb_{0.50}O_2$ pattern.

The impurity crystals with Nb/Ti $\simeq$ 3.60 comprised up to about 25% of a total of 32 crystals examined, and they probably correspond to the limiting composition of the Me_3O_7 solid solution. Other impurity crystals, having a mean Nb/Ti ratio of 5.39, might be transient intermediate phases. High-resolution microscopy observations (below) confirm that crystals of metastable, transient phases are indeed present in this system. These speculations regarding the nature of the impurity crystals in specimen $MeO_{2.375}$ are also consistent with its location near to the univariant triangle region. Similarly, the tie line for log p_{O_2} (atm) = -9.6 is determined from the microanalysis of a reduced $Ti_2Nb_{10}O_{29}$ specimen with O/Me = 2.344. The great majority of crystals examined in this specimen had Nb/Ti $\simeq$ 9.09 which is consistent with $Ti_{1.19}Nb_{10.81}O_{29}$ solid solution. This tie line indicates the equilibrium presence of $Ti_{1.19}Nb_{10.81}O_{29}$ with $Ti_{0.50}Nb_{0.50}O_2$, and further predicts the presence of an isobarically reduced $TiNb_2O_7$ sample having O/Me = about 2.14, which was verified experimentally. Like the previous sample, this one also contains crystals with differing Nb/Ti ratios which are probably a residue from the transition through the univariant region. For the highly reduced part of the diagram, microanalysis of two isobarically reduced $TiNb_2O_7$ and $Ti_2Nb_{10}O_{29}$ oxides at log p_{O_2} (atm) = -10.3 showed that the constituent phases in both specimens are located consistently along one tie line. Similarly, the tie line for log p_{O_2} (atm) = -10.8 was determined from the analysis of a reduced $Ti_2Nb_{10}O_{29}$ specimen $MeO_{2.215}$ which contained almost equal proportions of $Ti_{0.76}Nb_{11.24}O_{29}$ and $Ti_{0.27}Nb_{0.73}O_2$, again showing good collinearity between the oxygen/total metal ratio and the compositions of the $Me_{12}O_{29}$ and MeO_2 phases. The tie line also indicates that reduction of $TiNb_2O_7$, and probably also that of $Ti_2Nb_{10}O_{29}$, is complete before $Me_{12}O_{29}$ is thoroughly denuded of titanium. Finally at log p_{O_2} (atm) = ca. -11.4 reduction of $Ti_2Nb_{10}O_{29}$ is almost complete since microanalysis of specimen $MeO_{2.005}$ confirmed the presence of $Ti_{0.17}Nb_{0.83}O_2$. It is worthwhile to note that in all the oxides in which the rutile phase composition could directly be detected, the Nb/Ti ratios appeared to be homogeneous ($\pm$1–2% Ti) from one crystal to the next independent of the manner of their formation. This may indicate that the Ti–Nb distribution at 1400°C is equilibrating.

II. High-Resolution Transmission Electron Microscopy

To correlate the microstructural features of the reduced titanium–niobium oxides with their thermodynamic behavior, reduced $TiNb_2O_7$ specimens at different stages of reduction were investigated. The conclusion drawn from this study is also applicable to that of the reduced $Ti_2Nb_{10}O_{29}$ system, since there is a close analogy between the reduction behavior of the two oxides. Electron microscopy confirmed that the structure of the starting material, i.e., $TiNb_2O_7$, persisted in all the intermediate oxides taken from the first stage of the bivariant reduction. $TiNb_2O_7$ has a column structure with blocks of (3 $\times$ 3) octahedra wide, linked into finite ribbons by octahedra edge sharing (Fig. 3a). The structure can be symbolized $(3 \times 3)_\infty$ with a unit cell measuring a = 20.44 Å, b = 3.80 Å, c = 11.93 Å, and β = 120°10′ (*2*). An idealized

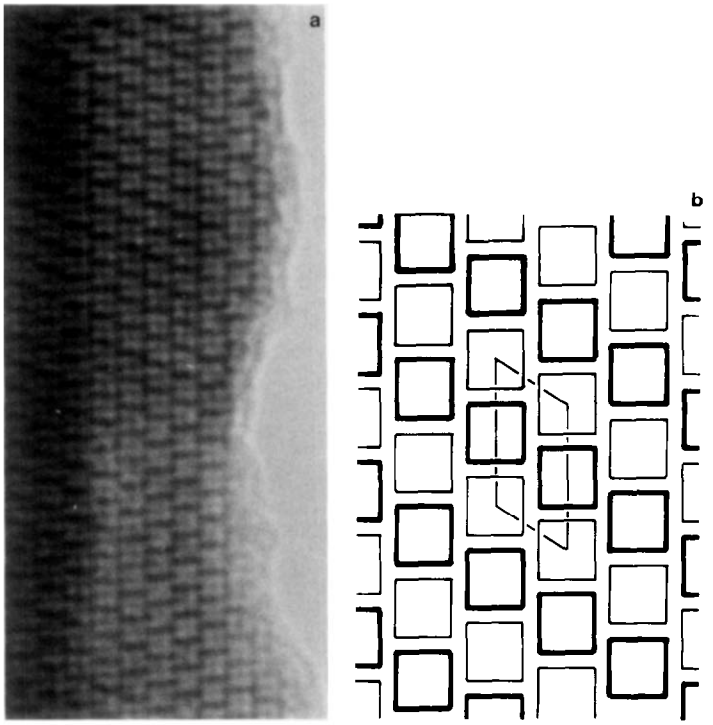

FIG. 3. (a) An electron micrograph of $TiNb_2O_7$. (b) An idealized model of $TiNb_2O_7$ showing the unit cell outline.

model in its simple representation is shown in Fig. 3b. Similarly, in the second stage of the bivariant reduction of $TiNb_2O_7$, the presence of the orthorhombic $Me_{12}O_{29}$ structure was encountered. The orthorhombic modification of the $Me_{12}O_{29}$ phase, i.e., $Ti_2Nb_{10}O_{29}$–$Nb_{12}O_{29}$ solid solutions, consists of blocks of (3 × 4) octahedra wide, connected in a zig-zag arrangement by octahedra edge sharing (Fig. 4a). Alternate blocks in the *b*-axis direction give an axial length of $b = 3.80$ Å, with $a = 28.5$ Å and $c = 20.5$ Å (*2*). An idealized model of this structure is shown in Fig. 4b. In the vicinity of the univariant triangle area, where the Me_3O_7 phase transforms to $Me_{12}O_{29}$, single crystals exhibited coherent intergrowth of the two structures. This is due to the fact that the two structures are related by a homologous series of oxides having a general formula $Me_{3n}O_{8n-3}$ (*Me* = metal atom), and with Nb_3O_7F as the parent compound (*17*). Figure 5a shows such a crystal fragment in which occasional files of Me_3O_7 structure (↑ A) are intergrown coherently with a predominantly $Me_{12}O_{29}$ structure. This crystal fragment was taken from specimen $MeO_{2.200}$ at $\log p_{O_2}$ (atm) = −9.30. In addition, the micrograph shows that (3 × 4) blocks of the $Me_{12}O_{29}$ phase are arranged, at least locally, in a monoclinic configuration. Because the monoclinic modification of $Me_{12}O_{29}$ is a low-temperature phase, the occurrence of this structure together with the remnant of the Me_3O_7 phase, i.e., strips of (3 × 3) blocks, may suggest that partial transformation from one phase to the other takes place via the formation of a *m*-$Me_{12}O_{29}$ precursor. An idealized model for the intergrowth is given

in Fig. 5b, in which the monoclinic unit cell of $Me_{12}O_{29}$ is outlined, measuring a = 20.50 Å, b = 3.80 Å, c = 15.37 Å, and β = 114° (*18*).

We also found in specimen $MeO_{2.200}$ a single crystal showing a new block structure compound (Fig. 6). The structure is suggestive of a reaction mechanism in the transformation of $TiNb_2O_7$ to o-$Me_{12}O_{29}$ solid solution by elimination of the rutile phase, MeO_2. In Fig. 6, blocks with (3 × 3) and (4 × 3) octahedra in cross section are clearly outlined. Within each block, individual (NbO_6) octahedra positions (~4 Å) are resolved and they appear as dark dots. Empty square channels (0.28 nm wide) between corner-sharing (NbO_6) octahedra are imaged as white dots. At the interface between (3 × 3) and (4 × 3) blocks, where the octahedra groups overlap in projection, metal atoms are not resolved and appear as elongated dark lines. These lines represent ordinary shear planes (*CS*) in which cations are 2 Å apart. The micrograph, in addition, shows unusual 6-Å-wide dark bands parallel to [100], which extend from the thin edge (about 10–20 Å) into the bulk of the crystal, separating strips of (3 × 3) and (4 × 3) blocks regularly. The relatively high contrast of these bands is attributed to a local increase in metal atom density. Distinct white spots located between each pair of blocks, on these bands, are surmized to represent empty tunnels running through the crystal, parallel to [010]. Where the crystal is thicker (i.e., in the lower part of the micrograph) the above characteristic image features are less clear, due to strong dynamical scattering of electrons (*19*).

The above intuitive interpretation of im-

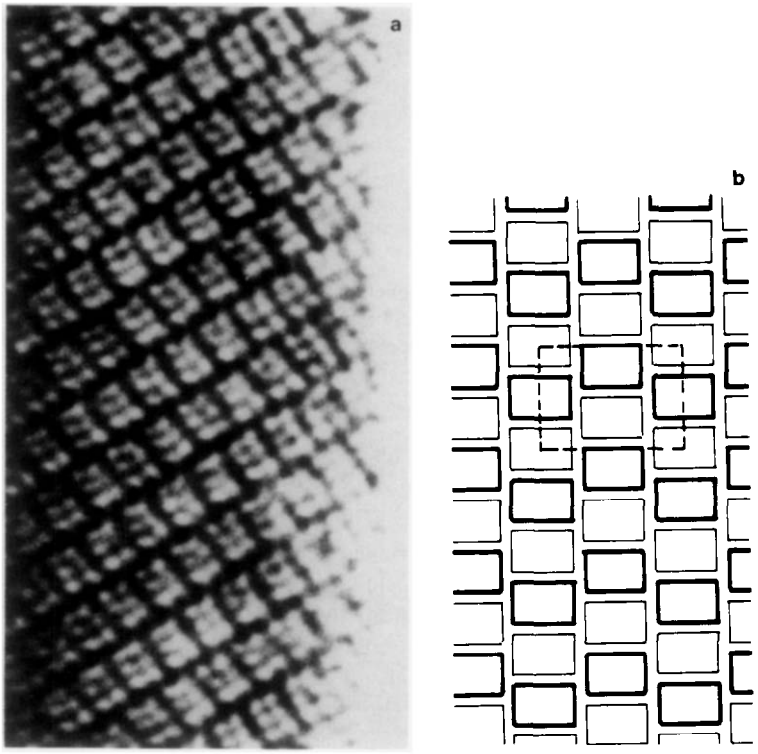

FIG. 4. (a) An electron micrograph of $Ti_2Nb_{10}O_{29}$. (b) An idealized model of $Ti_2Nb_{10}O_{29}$ showing the unit cell outline.

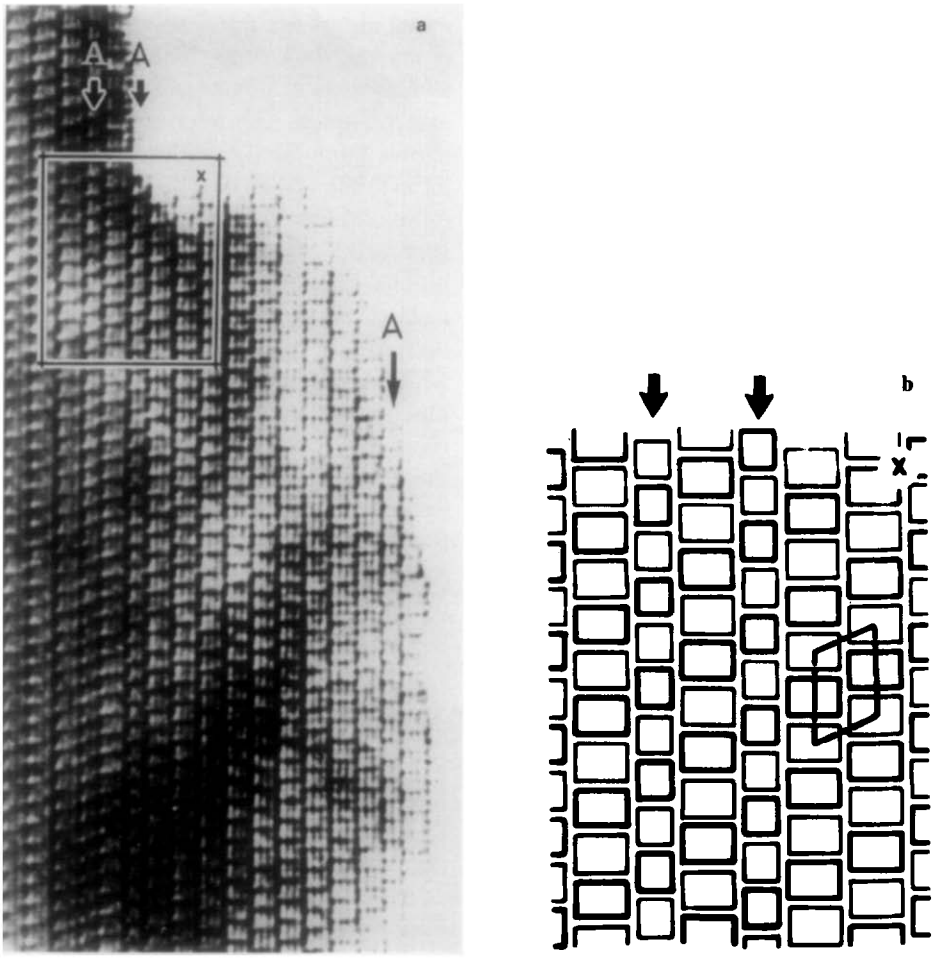

FIG. 5. (a) An electron micrograph from reduction product $MeO_{2.200}$, showing coherently intergrown lamellae of Me_3O_7 (↑ A) in the predominantly m-$Me_{12}O_{29}$ structure. (b) An idealized model of area showing a monoclinic $Me_{12}O_{29}$ structure with coherently intergrown (3 × 3) blocks of Me_3O_7 (↑). The unit cell of m-$Me_{12}O_{29}$ structure is outlined.

age contrast in Fig. 6 is based on the assumption that in a thin (<10 nm) region of the crystal a projection of the potential distribution is realized, i.e., the image corresponds in a one-to-one manner with the crystal structure. Factors influencing such "optimal" imaging have extensively been discussed in the literature (*20*). Previously, Fejes *et al.* (*21*) have demonstrated how the crystal structure image changes with the degree of objective lens defocus and aberrations, with crystal orientation, and with the resolution power of the microscope. Their data suggest that with an optimum defocus of about −90 nm and a resolution limit of about 0.35 nm for 100-kV electrons, there is a maximal thickness limitation of 15 nm, which corresponds to the range of phase–object approximation. However, in their opinion, under more suitable conditions recognizable images still can be obtained even in the case of high thicknesses. Experimental conditions in the present work (Section III) comply with the "optimal"

standard procedures given by the above authors. In addition, we have compared our structural observations (Fig. 6) with a throughfocus series of calculated image intensities in Fig. 9. The latter figure represents a proposed structure model which is described below:

In Fig. 7, an idealized model (A and B) shows alternative arrays of (5 × 3) and (4 × 3) blocks at the same level. The blocks overlap in every other common intergrowth plane, thus giving rise to the formation of rectangular tunnels with 5.6 × 2.8 Å^2 dimensions. Parallel to the [010] direction, the tunnels extend through the crystal with repeat distances of 10 and 22 Å along the *a* and *c* axes, respectively. The metal atom density in the overlapped region of the blocks, i.e., the 6-Å-wide band, has clearly increased and this most likely is the reason for the very distinct dark contrast observed in the crystal image (D). Quantitative verification of the image intensity in (D) and in Fig. 6, is shown in (C). Details of this calculation are described further below. The chemical composition of the structure, as calculated from the idealized model, is $Me_{25}O_{60}$ which can be expressed by the relation

$$Me_{25}O_{60} = 2(Me_{12}O_{29}) + MeO_2. \quad (3)$$

Equation 3 suggests that the units of the diffusing species, i.e., MeO_2, are incorpo-

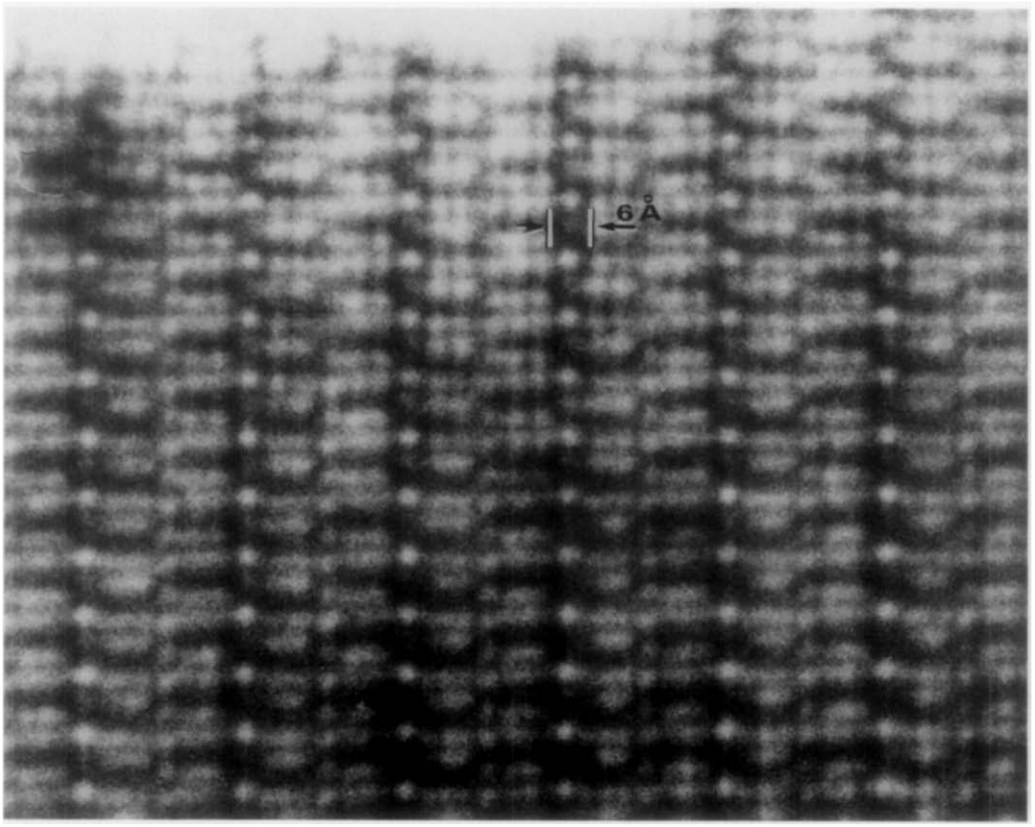

FIG. 6. Electron micrograph from reduction product $MeO_{2.200}$. The crystal structure reveals anomalous 6-Å-wide dark contrast bands running into the crystal, parallel to the $(100)_{ReO_3}$ plane. White contrast dots occur on these bands with a regular periodicity.

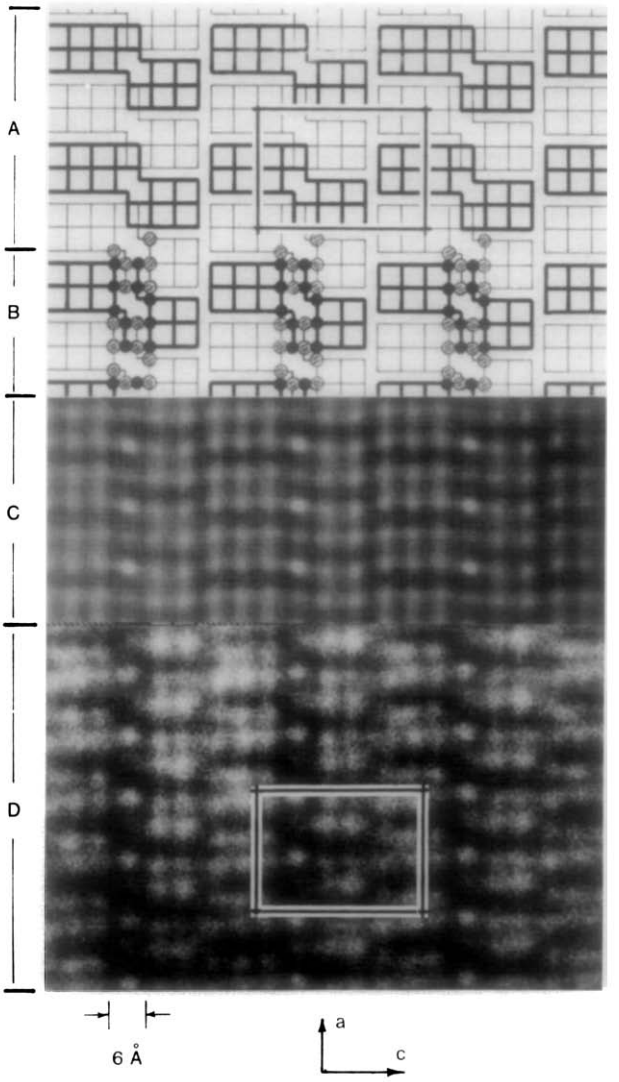

FIG. 7. (A and B) Structure model of the crystal shown in Fig. 6 and given in higher magnification in (D). (C) Stimulated high-resolution image of the structure. The unit cell of the structure is outlined both in the idealized model (A) and on the micrograph (D). The composition is $Me_{25}O_{60}$.

rated in the structure of the other phase, $Me_{12}O_{29}$. The $Me_{25}O_{60}$ superstructure is a metastable transient phase, generated in the reduction of $TiNb_2O_7$ to o-$Me_{12}O_{29}$ and a rutile phase, in the second bivariant stage. Evidence for its formation was found in one out of many crystal fragments examined. Such infrequent observation of transient structures most likely is due to fast kinetics of the reduction reaction at the isotherm studied. In reductions of titanium–niobium oxides at 1400°C, gas–solid equilibrium is attained in less than 1 hr, indicating that initial stages of structural rearrangements to transient intermediate phases take place rapidly, i.e., the structures are short-lived and transform instantaneously to stable phases. In the course of the reduction, dif-

fering species (Me^{4+} = Ti^{4+}, Nb^{4+}) are progressively generated within the parent block structure, which itself undergoes rearrangement. The altervalent cations subsequently segregate in an ordered manner on specific crystallographic sites in the parent structure. In Fig. 6, it is this aspect of the crystal reaction which is prominent. The heterogeneous formation of the second product phase (MeO_2) implies an outward flux of both cations and oxygen atoms, which diffuse through the crystal to the surface. Once on the crystal surface, the particles recombine to form nuclei of the heterogeneous phase, which subsequently grows to form a separate crystal. A plausible chemical mechanism underlying the diffusion process of MeO_2 units and the formation of o-$Me_{12}O_{29}$ is shown in Fig. 8a. In model (*e*), the structural element of $Me_{25}O_{60}$ is depicted; (*f*) and (*g*) represent subsequent atomic reshuffling leading to the generation of o-$Me_{12}O_{29}$ and a rutile phase (MeO_2). The locus of the reaction, according to this mechanism, is effectively confined. In model (*e*), a [010] string of atoms (· · ·–O–Me–O–Me–O–· · ·) labeled *b*, in a cooperative displacement by a_R through a short diffusion path, i.e., a_R $\langle 101 \rangle_R$, occupies the vacant position in the rectangular tunnel in its vicinity (labeled 3). Concurrently, the adjacent metal atom (labeled *a*) together with two free oxygen atoms, located in the apex of the octahedra (*a* in model *f*), diffuses out of the crystal through the 0.38-nm diagonal channels of the ReO_3 structure (1 and 2 in model *e*). The channels extend without interruption down the *b* axis. Diffusion normal to the *b* direction is impeded by changes of level at the interfaces between columns. Moreover, such diffusion across an interface is likely to be a highly activated and slow process. The proposed diffusion process parallel to the *b* axis is supported by findings of Sheasby and Cox (*22*), who reported that the chemical diffusion of oxygen in H-Nb_2O_5 at high temperature is highly anisotropic and takes place preferentially along the *b* axis. The mechanism proposed for the transformation of $Me_{25}O_{60}$ to o-$Me_{12}O_{29}$ and a MeO_2 unit further suggests that the altervalent cations, namely, Ti(IV) and Nb(IV), are segregated preferentially in the corner sites of the blocks. This finding is in agreement with results of von Dreele and Cheetham (*6*), who determined the crystal structure of $TiNb_2O_7$ and $Ti_2Nb_{10}O_{29}$ by the neutron diffraction method. They found that the lower valence cation Ti(IV) occupies mainly the block corners and they estimated the occupancy as 64.5% Ti for corner sites of $TiNb_2O_7$ and 40.0% Ti in corner positions of o-$Ti_2Nb_{10}O_{29}$.

The proposed reaction mechanism implies that in the course of the reduction, the transport of matter and block rearrangements within the crystal take place concurrently. That is, the heterogeneous formation of the rutile phase is accompanied by the quasihomogeneous transformation of the block structure phase to the related o-$Me_{12}O_{29}$ compound. This can be seen in Fig. 8b, showing a local domain of the crystal in which $Me_{25}O_{60}$ and o-$Me_{12}O_{29}$ structures coexist (labeled M and N, respectively). Deposition of the rutile phase in the small and very thin edge N is complete but in domain M and also in the rest of the crystal, the $Me_{25}O_{60}$ superstructure remains. This is evident from a change of the 6-Å-wide dark contrast band to an ordinary 2-Å spacing shear plane ($\uparrow$S). The crystal thickness in domain M is estimated to be less than 50 Å. This assumption is based on the fact that the contrast of the structure in M is consistent with the calculated image intensity distribution for this thickness (see Fig. 9). A structure model for the intergrowth area is shown in Fig. 8c in which columns of corner-sharing (MeO_6) octahedra are spliced together at two levels, $y = 0$ and $y = \frac{1}{2}b$. The model suggests a regular intergrowth boundary along $(001)_{ReO_3}$ which is an idealization.

The characteristic rectangular tunnels

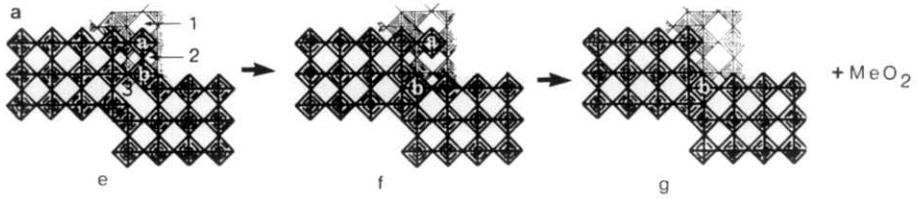
a
1
2
3
e
f
g
+ MeO2

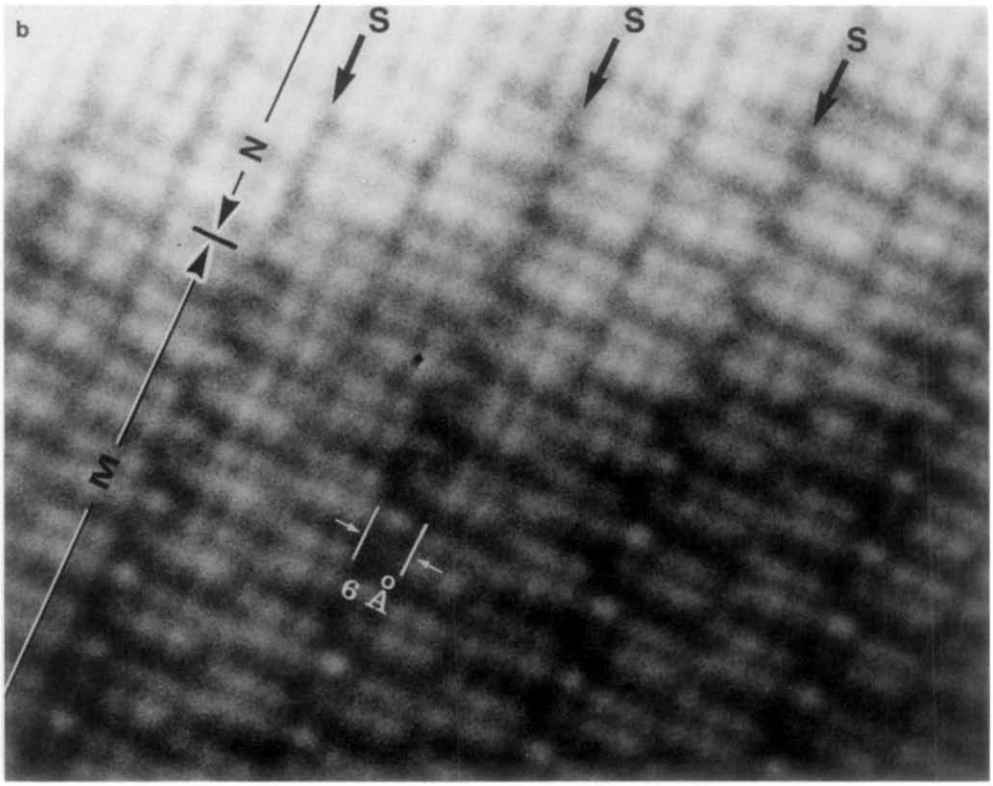
b
S
S
S
N
M
6 A°

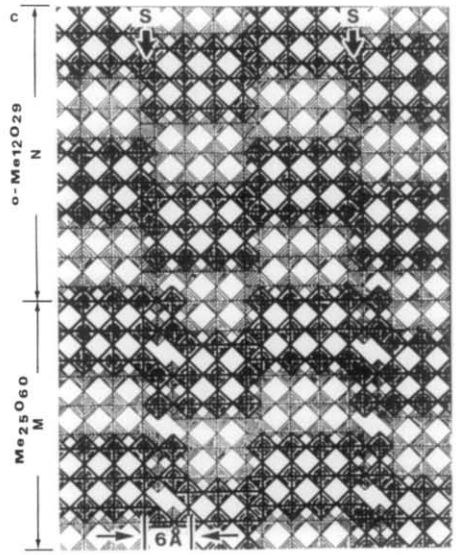
c
S
S
o-Me12O29
N
Me25O60
M
6A

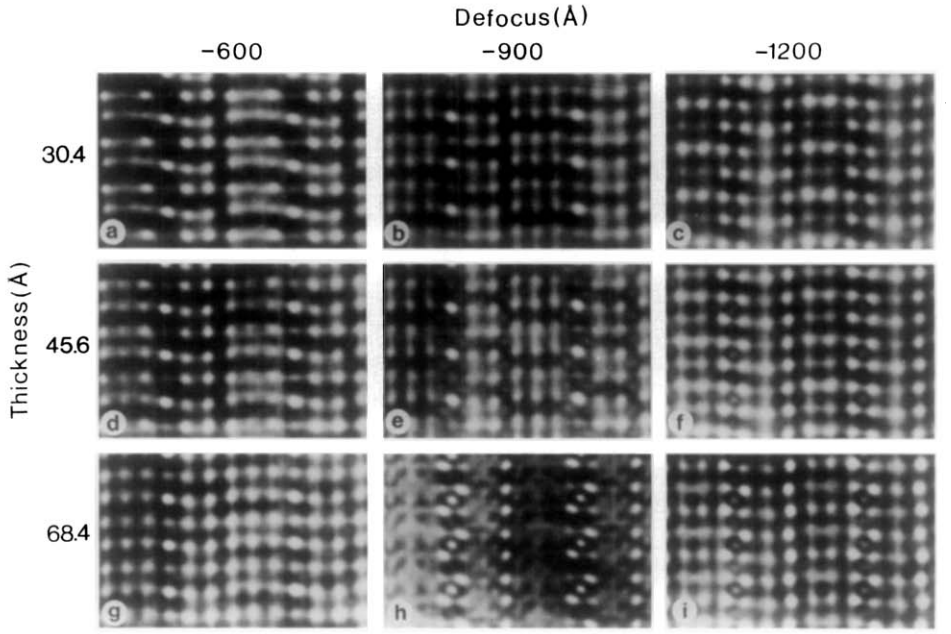

FIG. 9. Calculated lattice images of the $Me_{25}O_{60}$ structure under different defocus and thickness conditions. The best direct interpretable image appears to be at −90 nm defocus, with a thickness of 30.4 Å.

(5.6 × 2.8 Å^2) in the $Me_{25}O_{60}$ superstructure would appear to be a common feature in metastable block structure oxides. Similar tunnels have been observed in intermediate oxides generated by polymorphic transformation of B-Nb_2O_5 (*23*). The partial ordering of such tunnels recently has been reported for reoxidation products of both monoclinic and orthorhombic modifications of pure $Nb_{12}O_{29}$ oxides (*24*).

Also our interpretation of the 6-Å-wide dark bands as stemming from closely spaced and unresolved arrays of metal atoms is in accordance with literature data. For example, electron microscopy of hyperstoichiometric $Nb_{12}O_{29}$ has shown regular occurrence of dark spots in the (4 × 3) block corners. The black spots were interpreted as displaced and unresolved metal atom rows along the incident beam direction (*25*). Likewise, the enhanced dark contrast at sites corresponding to the tetrahedrally coordinated metal atoms of $GeNb_9O_{25}$ structure were attributed to high-density metal atom rows (*26, 27*).

To determine the chemical compositions of $Me_{25}O_{60}$, $Me_{12}O_{29}$, and MeO_2 in Eq. (3), the Guinier X-ray powder diffraction pattern of specimen $MeO_{2.200}$ was studied. The pattern contained strong reflections of both the $Me_{12}O_{29}$ and MeO_2 equilibrium phases. Cell dimensions of the rutile phase, as measured from the Guinier pattern, corresponded to $Ti_{0.52}Nb_{0.48}O_2$ and this also can

FIG. 8. (a) A proposed mechanism for the transformation of $Me_{25}O_{60}$ into o-$Me_{12}O_{29}$ and a rutile phase (MeO_2); models (*e*), (*f*), and (*g*) show the necessary atomic movements. (b) An electron micrograph of the same crystal as shown in Fig. 6. In the micrograph, 6-Å-wide dark bands continue into 2-Å-wide dark lines (↑ S) (an ordinary *CS* plane), suggesting that the two structures, $Me_{25}O_{60}$ (region M) and o-$Me_{12}O_{29}$ (region N), are intergrown. (c) An idealized model for the intergrowth of $Me_{25}O_{60}$ (M) and o-$Me_{12}O_{29}$ (N) on the $(001)_{ReO_3}$ plane.

be deduced from a mathematical expression for the calculation of isobaric tie lines in the ternary phase diagram (Eq. (4), and given in Ref. (*7*)). For reduced titanium–niobium oxides, the relationship between the niobium content of the rutile phase and the equilibrium oxygen pressure is

$$x = 0.279 + 0.168(\log p_{O_2} - 8.0) - 0.0055(\log p_{O_2} - 8.0)^2. \quad (4)$$

The first stage of the reduction of $TiNb_2O_7$ to $Me_{25}O_{60}$ then can be formulated

$$TiNb_2O_7 = 0.03(Ti_{7.16}Nb_{42.84}O_{120}) + 1.50(Ti_{0.52}Nb_{0.48}O_2) + 0.20(O_2). \quad (5)$$

In the next stage, $Ti_{7.16}Nb_{42.84}O_{120}$ eliminates another MeO_2 unit, $Ti_{0.52}Nb_{0.48}O_2$, and is transformed into the ultimate equilibrium stable phase $Ti_{1.53}Nb_{10.47}O_{29}$ according to reaction

$$T_{7.16}Nb_{42.84}O_{120} = 4(Ti_{1.53}Nb_{10.47}O_{29}) + 2(Ti_{0.52}Nb_{0.48}O_2). \quad (6)$$

Combination of Eqs. (5) and (6) thus leads to a phase relationship for the reduction of 1 mole of $TiNb_2O_7$ at $\log p_{O_2}$ (atm) = −9.30, which can be expressed by the following reaction

$$TiNb_2O_7 = 0.12(Ti_{1.53}Nb_{10.47}O_{29}) + 1.56(Ti_{0.52}Nb_{0.48}O_2) + 0.20(O_2). \quad (7)$$

This overall reaction is also consistent with results of analytical electron microscopy of the reduced $Ti_2Nb_{10}O_{29}$ specimen ($MeO_{2.375}$) at $\log p_{O_2}$ (atm) = −9.27 (see Table III). We also note that the Nb/Ti ratio (5.98) of the $Me_{25}O_{60}$ intermediate phase given in Eq. (5) is very close to that of one of the impurity phases detected in the analytical measurements (Table II).

III. Lattice Image Calculations

The structure images of $Me_{25}O_{60}$ were calculated by means of the multislice method for dynamical electron scattering (*13, 14*). In the calculation the atomic positions in the structure model (Fig. 7) for $Ti_9Nb_{41}O_{120}$ were used. The crystal structure is monoclinic with a space group *Cm* and cell parameters a = 19.0 Å, b = 3.8 Å, c = 26.6 Å, α = 90°, β = 90°, γ = 78.5°. In the calculations Nb and Ti atoms were assumed to be distributed randomly. The atomic scattering factors were taken from Doyle and Turner (*28*), and the Debye–Waller factors employed in the calculations were 0.5 $Å^{-2}$ for Nb and Ti atoms, and 1.0 $Å^{-2}$ for oxygen atom. The accelerating voltage was 100 kV, and the size of the objective aperture was equivalent to a radius of 0.4 $Å^{-1}$ in reciprocal space. The semiangle of the beam divergence was 1.4 mrad, while the value of the spherical aberration coefficient was determined as 1.9 mm by comparing calculated and experimental images of known structures. In the calculations the effects of chromatic aberration were also taken into account by adding a virtual aperture "damping envelope" function (*29*). Dynamic electron scattering was calculated over 569 beams for the [010] projection. The slice thickness was 3.80 Å. In Fig. 9 calculated images for different defocus and crystal thicknesses are shown. The best simulated image appears to be at −900 Å defocus and a crystal thickness of about 30.4 Å, and this calculated contrast diagram was utilized in the discussion of the $Me_{25}O_{60}$ structure (Fig. 7). At the same defocus, crystals up to 50 Å thick give similar images. For thicker crystals, similar images can be calculated, but they arise at defocus less than −900 Å. In these images, tunnels appear as bright spots, while regions with high metal atom densities in projection result in high contrast. At −1200 Å, however, the image contrast reverses; that is, the tunnels show up as dark spots. For crystals thicker than 68.4 Å and a defocus value of −900 Å, there seems to be no simple relationship between the simulated contrast and the experimental charge density.

Figure 7, in which a comparison is given

of the structure model (A and B), the experimentally observed image (D), and the calculated structure (C), suggests that the proposed crystal structure for the $Me_{25}O_{60}$ compound is correct. This lends credence to our proposed reaction mechanism for the reduction of $TiNb_2O_7$.

Discussion

The results of our analytical electron microscopy study of reduced titanium–niobium oxides are in good agreement with data previously reported on the basis of X-ray powder diffraction analysis (*7*). The two techniques are complementary, each having advantages and limitations. Significant aspects of the applications of these two methods in quantitative phase analysis of complex mixtures are briefly outlined below:

The X-ray powder diffraction method provides average information, representative of the whole system. The method is applicable here when the rutile phase reflections are unambiguously detectable in the patterns. From measured cell parameters of the rutile phase, the corresponding compositions can be interpolated from data for the TiO_2–NbO_2 solid solutions; TiO_2–NbO_2 forms a continuous solid solution in which the normal rutile phase is retained to a maximum of about 85 mole% NbO_2 (*30, 31*). The composition of a solid solution of the block structure phases cannot be obtained directly from the X-ray powder patterns, but is determined indirectly from the composition of the coexisting rutile phase. However, in the early stages of the reduction of $TiNb_2O_7$, the rutile lines are too weak to be detected; for example, these lines are hardly detectable in the oxides MeO_x, $x > 2.29$ at $\log p_{O_2}$ (atm) > -8.0. Likewise, in the first stages of the bivariant reduction of $Ti_2Nb_{10}O_{29}$, where Me_3O_7 occurs in equilibrium with $Me_{12}O_{29}$, no direct quantitative phase relationships can be determined. In the case of highly reduced oxides, although the X-ray powder patterns contain strong rutile phase reflections, broadening of the lines and merging with the block structure patterns restrict accurate measurements of cell dimensions. In previous work (*7*), these problems were circumvented by relating the niobium content of the rutile phase to the corresponding equilibrium oxygen pressure (see Eq. (4)). Isobaric tie lines calculated in this way were consistent with other experimental data.

The microanalytical method, on the other hand, provides a complementary means of phase analysis by sampling the compositions of the phases present. The internal consistency of the results, as shown by the collinearity of the points determining the tie lines, demonstrate the analytical precision. Each point is independent, being determined either by microanalysis of the constituent phases or by gravimetric analysis of the whole specimen. Because the oxygen content of the individual phases, i.e., Me_3O_7, $Me_{12}O_{29}$, or MeO_2, cannot be monitored with a conventional X-ray detector, each Nb/Ti ratio had to be assigned to a particular phase on the basis of structural characterization by X-ray powder diffraction. In systems where all the elements can be observed by their X-ray emissions, the microanalytical method yields direct and unambiguous data.

A combination of analytical electron microscopy with high-resolution transmission electron microscopy clearly showed that the reduction of titanium–niobium oxides is a diffusion-controlled and, in part, a heterogeneous reaction. Under controlled oxygen fugacities both cations and oxygen atoms dissociate from the lattice sites of the original compounds and diffuse outward to the crystal surface. Recombination of the atoms on the surface of the crystals leads to the formation of a second product phase containing an initially higher Ti/Nb ratio

than the original block structure. Consequently, the block structure phase undergoes a phase transition to other oxides which are either isostructural phases in the binary Nb–O system or structurally related oxides occurring as lamellae or domains in the matrix of the host structure. As the reduction proceeds further, the density of the intergrowth structure progressively increases until the roles of the matrix and solute are reversed. Continuity in the phase transformation, hence, is preserved and thus the system simulates bivariant characteristics. Formation of the titanium-rich rutile phase in the initial stages of the reductions probably arises from the fact that TiO_2 ($\Delta G_f^0 = -888.7$ kJ · mole^{-1}) is considerably more stable than NbO_2 ($\Delta G_f^0 = -739.9$ kJ · mole^{-1}) (*32*).

The superstructure $Me_{25}O_{60}$ reported in the present work is a metastable phase generated in the direct transformation of $TiNb_2O_7$ to $Me_{12}O_{29}$ and a MeO_2 phase. Because the equilibrium in the reduction of titanium–niobium oxides is attained in less than 1 hr at 1400°C, the formation and subsequent conversion of the transient structure is likely to be rapid. In the present system, an intergrowth between the transient phase and a stable phase has yielded information on the mechanism of the reaction concerned. This phenomenon has also been noted in the generation of Wadsley defects, and their subsequent ordering as intergrowth phases, in the reduction of H-Nb_2O_5 below 1000°C (*23*). For further studies of intermediate metastable phases in the Ti–Nb–O system, it is recommended that oxides obtained from low-temperature reduction reactions be employed. Such oxides might contain an adequate number of crystals showing transient phases.

Acknowledgments

The foundation of this work was laid down through the collaboration (of SKEF) with Professor J. S. Anderson F.R.S. in the Inorganic Chemistry Laboratory, Oxford University, Oxford, U.K. Part of the study presented was carried out (in 1979) in the Department of Chemistry and the Department of Physics of Arizona State University, Tempe, Arizona where SKEF was supported by NSF Grant DMR 77-08473, and A.O. by NSF Grant DMR 80-02108. Both authors gratefully acknowledge Professor LeRoy Eyring for the opportunity to accomplish the work. We also thank the Science Research Council (U.K.) for the grant toward the purchase of an analytical electron microscope.

References

1. R. S. Roth and L. W. Coughanour, *J. Res. NBS* **55,** 209 (1955).
2. A. D. Wadsley, *Acta Crystallogr.* **14,** 660, 664, (1961).
3. R. Gruehn, and H. Schäfer, *Naturwissenschaften* **50,** 642 (1963).
4. R. S. Roth, A. D. Wadsley, and B. M. Gatehouse, *Naturwissenschaften* **51,** 262 (1964).
5. R. S. Roth, and A. D. Wadsley, *Acta Crystallogr.* **18,** 724 (1965).
6. R. B. von Dreele, and A. K. Cheetham, *Proc. R. Soc. London A* **338,** 311 (1974).
7. S. K. E. Forghany, and J. S. Anderson, *J. Solid State Chem.* **40,** 136 (1981).
8. S. K. E. Forghany, and J. S. Anderson, *J. Solid State Chem.* **40,** 143 (1981).
9. A. K. Cheetham, and A. J. Skarnulis, *Anal. Chem.* **53,** 1060 (1981).
10. S. K. E. Forghany, *J. Phys. E* **15,** 248 (1982).
11. G. Cliff, and G. W. Lorimer, *J. Microsc. (Oxford)* **103,** 203 (1975).
12. K. F. J. Heinrich, *in* "The Electron Microprobe" (T.D. Mckinley, K. F. J. Heinrich, and D. B. Wittry, Eds.), p. 350. Wiley, New York (1966).
13. J. M. Cowley, and A. F. Moodie, *Proc. Phys. Soc. B* **70,** 497 (1957).
14. P. Goodman, and A. F. Moodie, *Acta Crystallogr. A* **30,** 280 (1974).
15. M. A. O'Keefe, *Acta Crystallogr. A* **29,** 389 (1973).
16. S. Kimura, *J. Solid State Chem.* **6,** 438 (1973).
17. S. Andersson, *Acta Chem. Scand.* **18,** 2339 (1964).
18. R. Norin, *Acta Chem. Scand.* **20,** 871 (1963).
19. J. M. Cowley, *Annu. Rev. Phys. Chem.* **29,** 251 (1978).
20. Nobel Symposium 47: Direct Imaging of Atoms in Crystals and Molecules, Lidingö, Sweden, August 6–10, 1979 (L. Kihlborg, Ed.). Also in *Chem. Script.* **14** (1978–79).

21. P. L. FEJES, S. IIJIMA, AND J. M. COWLEY, *Acta Crystallogr. A* **29,** 710 (1973).
22. J. S. SHEASBY AND B. G. COX, *J. Less-Common Met.* **15,** 129 (1968).
23. S. K. E. FORGHANY, AND J. S. ANDERSON, *J. Chem Soc. Dalton Trans.*, p. 255 (1981).
24. VON B. MEYER, AND R. GRUEHN, *Z. Anorg. Allg. Chem.* **484,** 53, 77, 98 (1982).
25. S. IIJIMA, S. KIMURA, AND M. GOTO, *Acta Crystallogr. A* **30,** 251 (1974).
26. J. S. ANDERSON, D. J. M. BEVAN, A. K. CHEETHAM, R. B. VON DREELE, J. L. HUTCHISON, AND J. STRAHLE, *Proc. R. Soc. London A* **346,** 139 (1975).
27. A. J. SKARNULIS, S. IIJIMA, AND J. M. COWLEY, *Acta Crystallogr. A* **32,** 799 (1976).
28. P. DOYLE AND P. TURNER, *Acta Crystallogr. A* **24,** 390 (1968).
29. A. OLSEN AND J. C. H. SPENCE, *Philos. Mag. A* **43,** 945 (1981).
30. B. O. MARINDER AND A. MAGNELI, *Acta Chem. Scand.* **12,** 1345 (1958).
31. K. SAKATA, *J. Phys. Soc. Japan* **26,** 1067 (1969).
32. NBS Tech. Note (*U.S.*) **270,** Nos. 1–6 (1965).